nanomaterials

MDPI

Communication

Comprehensive Investigation of Constant Voltage Stress Time-Dependent Breakdown and Cycle-to-Breakdown Reliability in Y-Doped and Si-Doped HfO_2 Metal-Ferroelectric-Metal Memory

Ting-Yu Chang [1], Kuan-Chi Wang [1], Hsien-Yang Liu [2], Jing-Hua Hseun [3], Wei-Cheng Peng [1], Nicolò Ronchi [4], Umberto Celano [4,5], Kaustuv Banerjee [4], Jan Van Houdt [4,6] and Tian-Li Wu [1,2,3,*]

1 International College of Semiconductor Technology, National Yang Ming Chiao Tung University, Hsinchu 30010, Taiwan; emmatony11111.st10@nycu.edu.tw (T.-Y.C.); kcwang.st09@nycu.edu.tw (K.-C.W.); wcpeng.st11@nycu.edu.tw (W.-C.P.)
2 Institute of Electronics, National Yang Ming Chiao Tung University, Hsinchu 30010, Taiwan; hyliu.ee10@nycu.edu.tw
3 Institute of Pioneer Semiconductor Innovation, National Yang Ming Chiao Tung University, Hsinchu 30010, Taiwan; jhhsuen.10@nycu.edu.tw
4 Imec, 3000 Leuven, Belgium; nicolo.ronchi@imec.be (N.R.); umberto.celano@asu.edu (U.C.); kaustuv.banerjee@imec.be (K.B.); jan.vanhoudt@imec.be (J.V.H.)
5 School of Electrical, Computer and Energy Engineering, Arizona State University, Tempe, AZ 85287, USA
6 Department of Physics and Astronomy, KU Leuven, 3000 Leuven, Belgium
* Correspondence: tlwu@nycu.edu.tw

Citation: Chang, T.-Y.; Wang, K.-C.; Liu, H.-Y.; Hseun, J.-H.; Peng, W.-C.; Ronchi, N.; Celano, U.; Banerjee, K.; Van Houdt, J.; Wu, T.-L. Comprehensive Investigation of Constant Voltage Stress Time-Dependent Breakdown and Cycle-to-Breakdown Reliability in Y-Doped and Si-Doped HfO_2 Metal-Ferroelectric-Metal Memory. *Nanomaterials* **2023**, *13*, 2104. https://doi.org/10.3390/nano13142104

Academic Editor: Alexander Tselev

Received: 12 June 2023
Revised: 14 July 2023
Accepted: 14 July 2023
Published: 19 July 2023

Abstract: In this study, we comprehensively investigate the constant voltage stress (CVS) time-dependent breakdown and cycle-to-breakdown while considering metal-ferroelectric-metal (MFM) memory, which has distinct domain sizes induced by different doping species, i.e., Yttrium (Y) (Sample A) and Silicon (Si) (Sample B). Firstly, Y-doped and Si-doped HfO_2 MFM devices exhibit domain sizes of 5.64 nm and 12.47 nm, respectively. Secondly, Si-doped HfO_2 MFM devices (Sample B) have better CVS time-dependent breakdown and cycle-to-breakdown stability than Y-doped HfO_2 MFM devices (Sample A). Therefore, a larger domain size showing higher extrapolated voltage under CVS time-dependent breakdown and cycle-to-breakdown evaluations was observed, indicating that the domain size crucially impacts the stability of MFM memory.

Keywords: ferroelectric; domain size; reliability

1. Introduction

Since the initial discovery of Si-doped HfO_2 materials' ferroelectric properties in 2011 [1], significant attention has been directed toward oxide materials with a fluorite structure, such as doped HfO_2 [2], and the solid solution of $Hf_xZr_{1-x}O$ (HZO) [3]. These materials have garnered interest for their compatibility with advanced process technology and ability to exhibit ferroelectric behavior even at thicknesses of $\leq$10 nm, setting them apart from traditional perovskite ferroelectric materials. Recent studies have revealed that the thickness of HfO_2-based ferroelectric films can be reduced to as little as 1 nm while maintaining the occurrence of spontaneous polarization and its ability to alter polarization direction [4]. This finding suggests that HfO_2-based ferroelectric film does not have a critical threshold for scaling down, unlike perovskite materials. This exceptional scalability feature indicates a promising advantage for developing memory devices driven by polarization.

Furthermore, ferroelectric HfO_2-based technologies are promising materials for non-volatile memories [5], logic FETs [6], and neuromorphic applications [7–9] because of their compatibility with complementary metal-oxide-semiconductor (CMOS) technology [10,11]. Ferroelectric properties can be induced by various doping species in HfO_2 films,

e.g., Zr, Si, Al, Gd, etc. Recently, high-performance ferroelectric-based technologies have been demonstrated with optimized annealing conditions, dopants, electrodes, interfacial layers, etc. [12–21]. However, reliability remains one of the main concerns in ferroelectric-based technologies [22], particularly the instability related to domain size's impact on time-dependent dielectric breakdown and cycle-to-breakdown. Understanding the impact of domain size on the stability of ferroelectric-based devices is not extensively reported in the literature.

In this study, Yttrium (Y)-doped and Silicon (Si)-doped HfO_2 metal-ferroelectric-metal (MFM) devices were fabricated to intentionally induce different domain sizes in metal-ferroelectric-metal (MFM) devices. The o-phase with ferroelectricity can be induced through the annealing process of differently doped ferroelectric films since the crystal radius of doping below/above Hf can stabilize the t-/c-phases [2]. CVS time-dependent stress and cycle-to-breakdown measurements were conducted. Furthermore, the correlations between domain size and CVS time-dependent stress and cycle-to-breakdown stability are discussed and analyzed to understand the impact of domain size.

2. Materials and Methods

Figure 1 shows the schematic structure of metal-ferroelectric-metal (MFM) capacitors and a brief process flow of this work. At first, 10-nm TiN was deposited via PVD as the bottom electrode. Next, 9.5-nm HfO_2-based ferroelectric layers with two different dopants, Y and Si, were deposited via thermal ALD at 300 °C. Afterward, another 10-nm TiN was deposited via ALD on the ferroelectric films as the top metal electrode. Lastly, RTA was conducted in N_2 ambient at 650 °C for crystallization for 20 s.

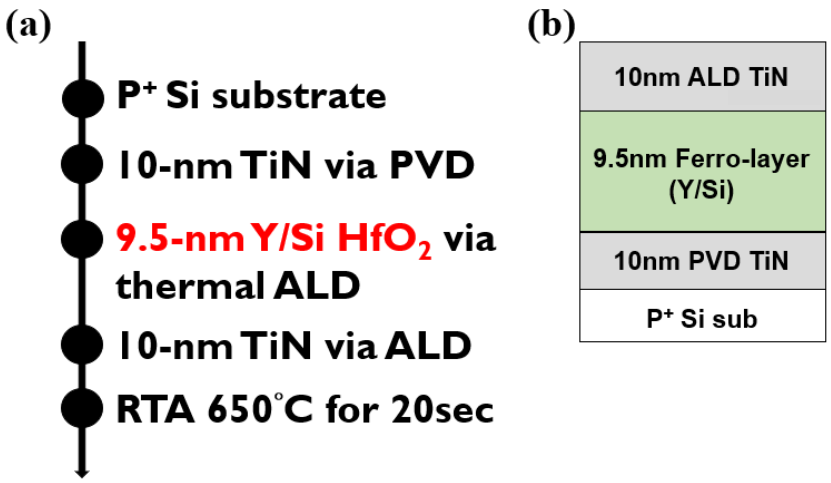

Figure 1. (**a**) Schematic of the process flow and (**b**) schematic structure of MFM capacitors with different dopants in ferroelectric layers.

The measurement setup for the capacitor used in this study was 2400 μm^2 (60 $\mu m \times 80$ μm). To perform electrical characterizations such as I-V (current-voltage) and time-dependent dielectric breakdown (TDDB) measurements, a Keysight B1500 Source Measurement Unit (SMU) Keysight, USA, was employed. To characterize the ferroelectric properties, including P-V (polarization-voltage) and cycle-to-breakdown measurements, a Keysight B1530 Waveform Generator/Function Measurement Unit (WGFMU) Keysight, USA, was utilized. In this setup, the capacitor was biased at the bottom via a chuck electrode, while a ground electrode was placed on top.

To compare the sample's domain size, distribution, and homogeneity, we used contact resonance piezoresponse force microscopy (PFM). Although a quantitative interpretation of the results is beyond the scope of this work, we used the same probe. We also operated under the same conditions on two samples with the same physical thickness (9.5 nm). Therefore, the results represent a relative comparison between samples and can be used

to analyze the domain size (Figure 2). For instance, Sample A (Y-doped) has a smaller domain size than Sample B (Si-doped). Details of the domain structures can also be found elsewhere [23]. Table 1 briefly describes the dopants and domain sizes used in this study. Distinct differences in the domain sizes of Sample A and Sample B can be used to understand the impact of domain size on the reliability of MFM devices.

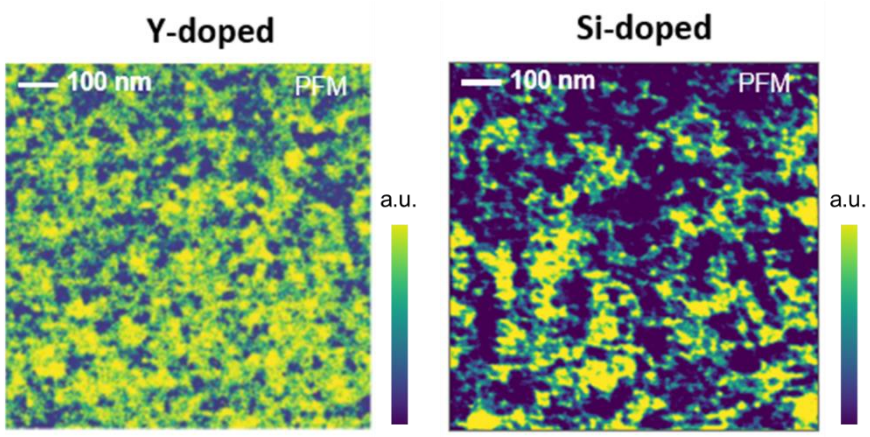

Figure 2. Contact resonance piezoresponse force microscopy PFM measurements in Sample A (Y-doped) and Sample B (Si-doped).

Table 1. A brief summary of the dopants and domain sizes used in this study.

	Dopant in Ferroelectric Layer	Domain Size (nm)	Doping Concentration
Sample A	Y	5.6	2.9%
Sample B	Si	12.5	2.5%

3. Results

To understand ferroelectricity, we used P-V measurements with a triangular pulse of 10 µs/V and a trapezoidal plus with T_r (rising time)/T_f (falling time) fixed at 0.5 µs and T_{width} (pulse width) set at 1µs for the cycling. Figure 3 shows the P-V characteristics of Samples A and B in the fresh state and after 10^3 cycles. Figure 4 shows comprehensive endurance characteristics at different cycling numbers. Sample A shows a slightly larger 2Pr than Sample B in the pristine state. Upon increasing the cycling number, Sample A exhibits a clear wake-up effect with a saturation of 2Pr after 10^4 cycles. However, Sample B does not exhibit a saturation of 2Pr. Overall, Sample A shows a larger 2Pr than Sample B after 10^5 cycles

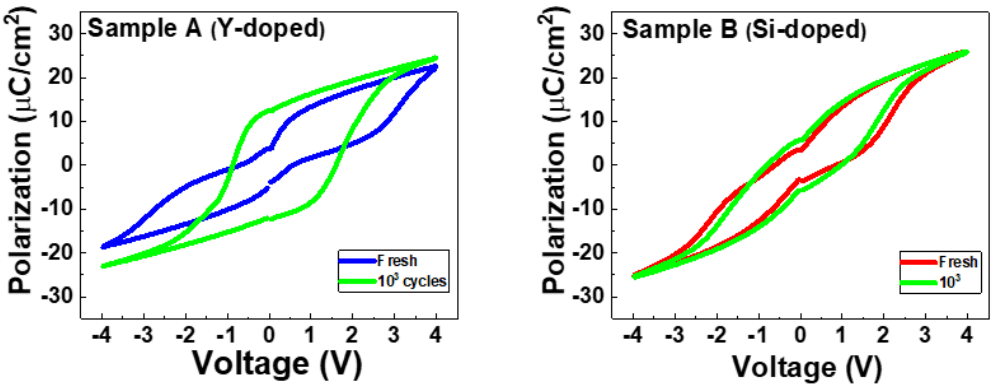

Figure 3. P-V characteristics in Samples A and B.

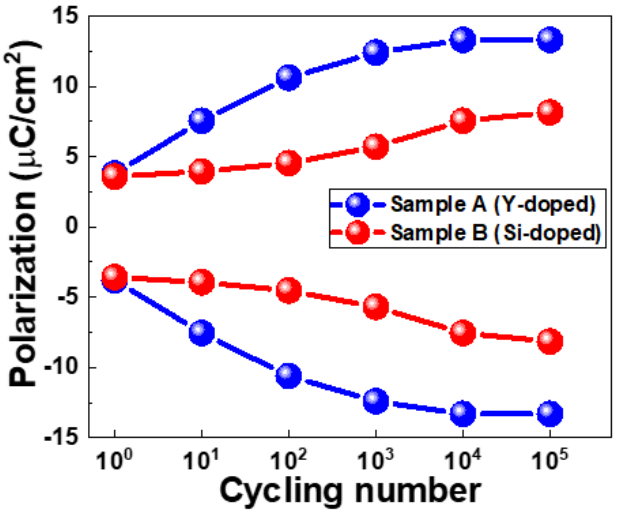

Figure 4. Polarization characteristics with respect to cycling numbers.

To understand the impact of domain size on time-dependent breakdown stability, we performed constant voltage stress time-dependent dielectric breakdown and cycling-to-breakdown evaluations. Figures 5 and 6 show the results of the constant voltage stress (CVS) time-dependent dielectric breakdown (TDDB) and cycle-to-breakdown evaluations in Samples A and B, respectively.

Figure 5c,d shows Weibull plots of time-to-breakdown (t_{BD}) distributions for three TDDB VG conditions, which follow the Weibull failure distribution:

$$\ln[-\ln(1 - F(t))] = \beta \ln(t) - \beta \ln(\eta) \quad (1)$$

where t is the time; β is the shape parameter; η is the scale factor of 63.2% value. The fitted β is 2.497 and 3.829 for Samples A and B, respectively. A higher β implies a tight distribution and small variability.

In Figure 5e, lifetime of 1% failure analyses are extrapolated from the Weibull plot of t_{BD} distribution and projected to a 10-year line. The operating voltages of Sample A are slightly lower than Sample B (2.62 V) at 2.24 V.

In designing the cycle-to-breakdown (Cycle-to-BD) measurement, we chose a PUND waveform with triangular pulses for the reading state. We set the rising, falling, and delay times ($T_r/T_f/T_{delay}$) to a fixed duration of 5 µs. The PUND waveform allowed for clear observation of whether or not the sample experienced breakdown. In the cycling state, trapezoidal pulses were used as the waveform. The T_r and T_f were fixed at 0.5 µs, while the T_{width} was set to 1 µs. To determine the cycles of the chosen reading step, we divided the interval to reach 1E6 cycles into 12 segments. After calculations, we determined that $10^{0.375}$ cycles would serve as the interval between the two consecutive reading states.

Similar to the TDDB analysis, cycle-to-breakdown (Cycle-to-BD) distributions for three different Cycle-to-BD VG conditions were used to construct Weibull plots. These plots were then used to extract fitting values from the ß value and generate lifetime curves. However, to adapt the Weibull failure distribution to the Cycle-to-BD analysis, the time-to-BD (t_{BD}) was transformed into cycle-to-BD (C_{BD}). Figure 6c,d display the fitting β values and corresponding lines for different devices. Sample A yielded a fitted β value of 0.948, while sample B had a βvalue of 1.274. These values are consistent with the TDDB analysis results, where Sample B exhibited a higher β value. The discrepancy in β values between TDDB and Cycle-to-BD measurements may be due to the Cycle-to-BD measurement using both positive and negative pulses during the cycling stage compared to TDDB measurements with a constant positive bias.

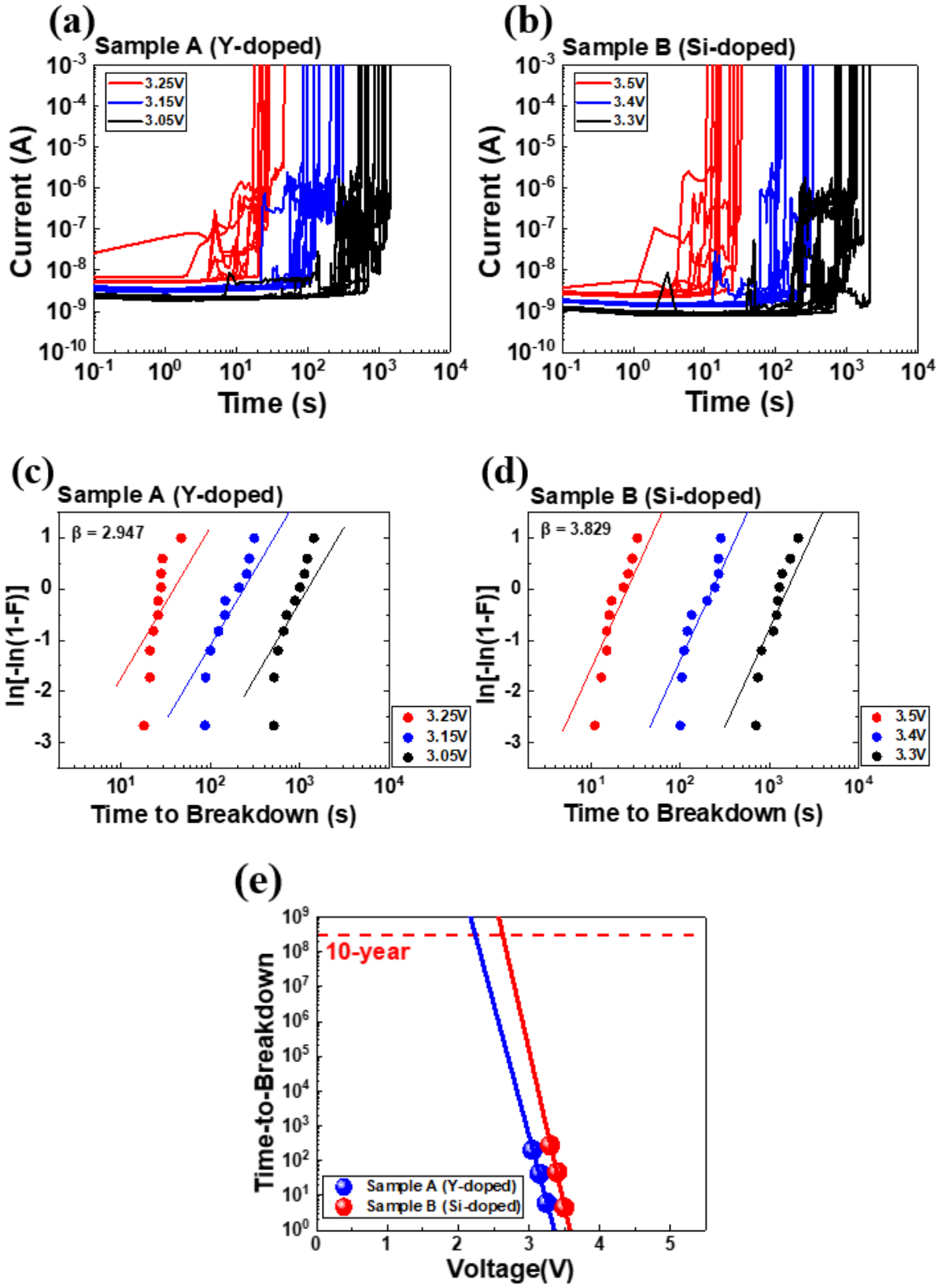

Figure 5. Gate current for (**a**) Sample A and (**b**) Sample B, as monitored by six different voltages (10 devices per group). (**c**,**d**) show corresponding Weibull plots of t_{BD}. (**e**) Operating voltage extrapolation for a 10-year lifetime at 1% failure for devices with Samples A and B.

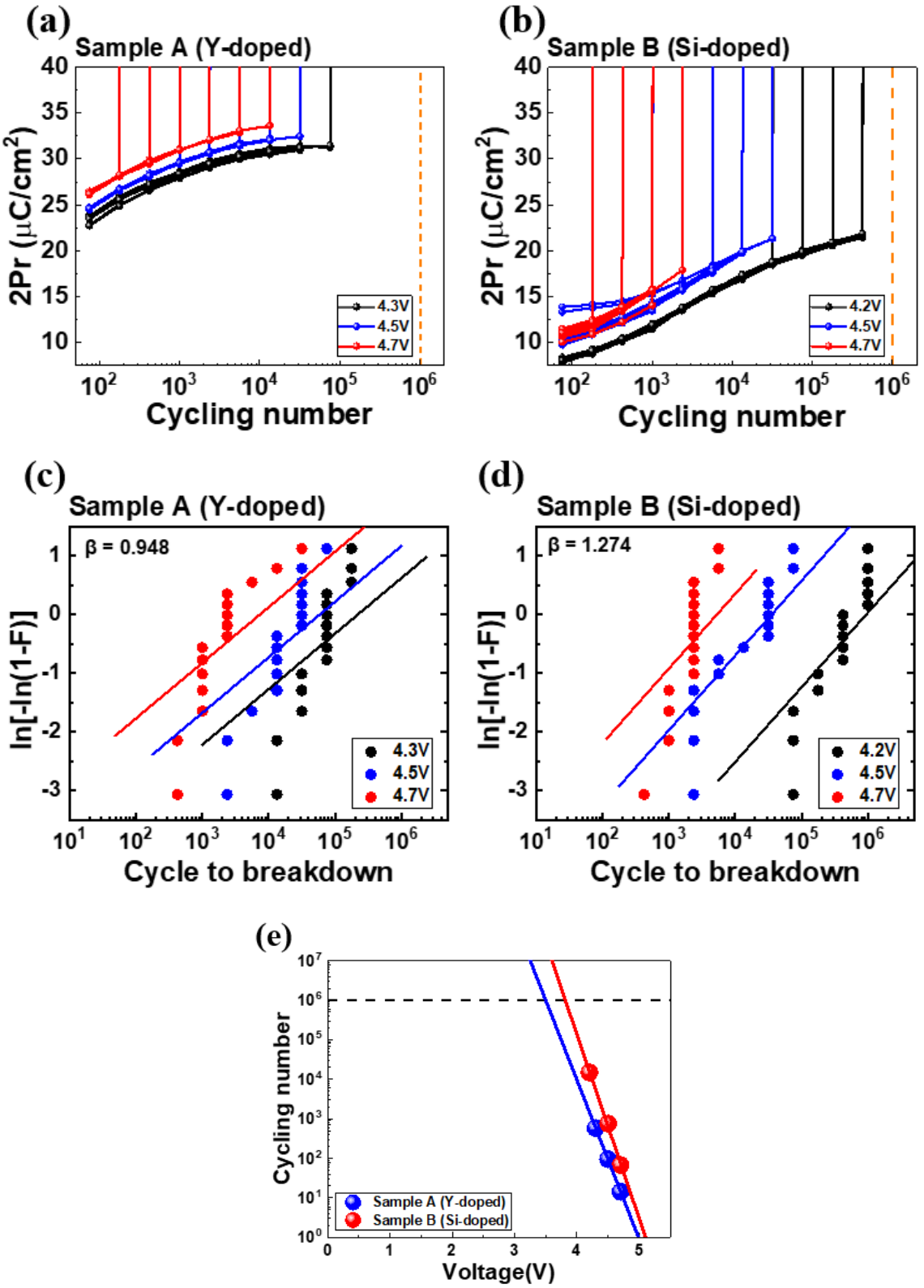

Figure 6. 2Pr for (**a**) Sample A and (**b**) Sample B, as monitored by six different voltages (10 devices per group). (**c**,**d**) show corresponding Weibull plots of cycle-to-breakdown. (**e**) Operating cycling number extrapolation for a 10^6-cycling lifetime at 1% failure for Samples A and B.

Figure 6e illustrates the 1% failure analysis of the 10^6-cycle lifetime analysis. The trend observed in the Cycle-to-BD analysis is similar to the TDDB analysis. For Sample A, the

determined operating voltage is 3.45 V, which is slightly lower than Sample B's operating voltage of 3.79 V.

Figure 7 shows the correlation between operation voltage (based on constant voltage stress TDDB and cycle-to-breakdown measurements) and domain size. Table 2 summarizes operation voltages based on CVS TDDB and cycle-to-breakdown evaluations. Figure 7 indicates that a larger domain size exhibits better TDDB and cycle-to-breakdown stability, i.e., higher 10-year operation voltages and higher voltages up to 10^6 cycles. In addition, Table 3 presents the maximum lifetime of targeting applied voltage at 3V results that Samples A and B can withstand in seconds. We calculated the lifetime of the Cycle-to-BD measurement by multiplying the predicted breakdown cycling number by a duration of 1 cycle in the measurement waveform design. According to our results, the lifetime measured in the TDDB analysis is longer than in the Cycle-to-BD analysis. This finding indicates that the measurement technique involving the continuous application of the same bias direction is less likely to induce defects generation and device breakdown than the technique involving a continuously changing bias direction. However, from the lifetimes in seconds, Sample B still exhibits a longer lifetime with a larger domain size in both the TDDB and Cycle-to-BD measurements. These findings are consistent with previous results.

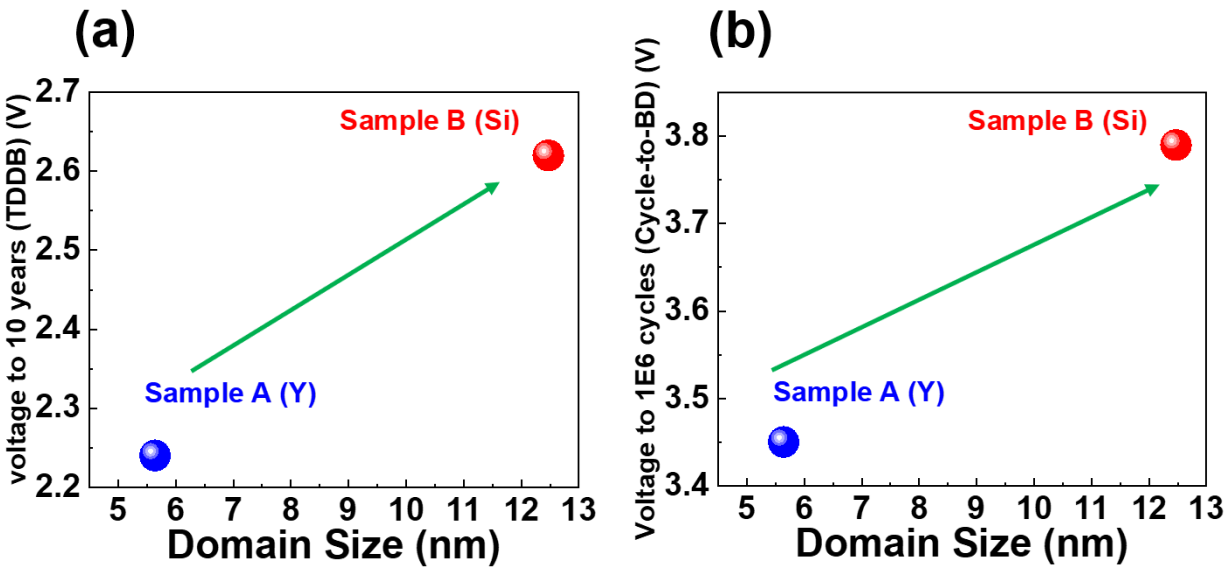

Figure 7. Extrapolated voltages vs. domain size under CVS TDDB (**a**) and cycle-to-breakdown measurements (**b**).

Table 2. Summary of the extrapolated operation voltage.

	10-year Operation Voltage Based on CVS TDDB	10^6-Cycling Operation Voltage Based on Cycle-to-Breakdown
Sample A	2.24	3.45
Sample B	2.62	3.79

Table 3. The maximum lifetime results that two samples can withstand in seconds.

	Lifetime of Cycle-to-BD @3V (s)	Lifetime of TDDB @3V (s)
Sample A	203	515
Sample B	12,170	146,058

The charging effects along the domain boundaries have been reported [24]. Therefore, larger domain sizes represent fewer domain boundaries (Figure 8) and reduce the chance of charging effects that create leakage paths as bias is applied to the device, thereby improving TDDB and cycle-to-breakdown stability. Besides, it is worth noting that Sample B exhibits larger β than Sample A, indicating better uniformity due to fewer domain boundaries in Sample B. In summary, larger domain sizes and fewer domain boundaries can improve CVS TDDB and cycle-to-breakdown reliability. However, samples with a larger domain size may degrade ferroelectricity.

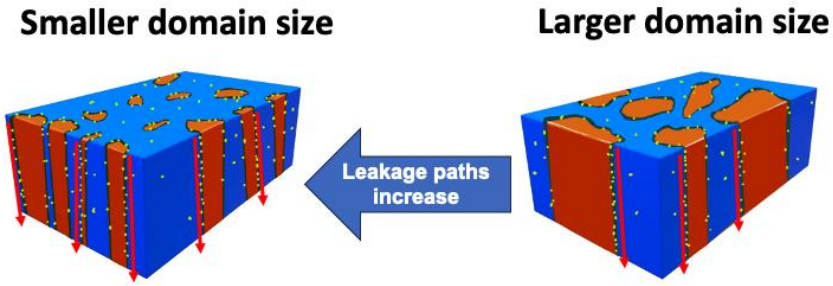

Figure 8. Schematic illustration of domain size's effect on the leakage path.

4. Conclusions

In this study, the impact of domain size on the constant voltage stress TDDB and cycle-to-breakdown reliability are systematically reported. Firstly, MFM devices were fabricated with two different dopants in the ferroelectric layer, which intentionally induced different domain sizes. The PFM analysis indicated that Sample B (Si-doped) had a larger domain size than Sample A (Y-doped). Furthermore, CVS TDDB and cycle-to-breakdown evaluations were conducted in Sample A and Sample B, indicating that Sample B had better CVS TDDB and cycle-to-breakdown stability. A clear correlation was observed between the larger domain size and better time-dependent stability, which may be attributed to fewer domain boundaries in Sample B. We are the first to report the effects of domain size on CVS TDDB and cycle-to-breakdown reliability and conclude that optimizing the domain size can improve devices' reliability.

Author Contributions: Conceptualization, T.-Y.C., K.-C.W. and T.-L.W.; methodology, T.-Y.C., K.-C.W. and T.-L.W.; formal analysis, T.-Y.C., K.-C.W., H.-Y.L., N.R., U.C. and T.-L.W.; investigation, T.-Y.C., K.-C.W., H.-Y.L., N.R., U.C. and T.-L.W.; data curation, T.-Y.C. and K.-C.W.; writing—original draft preparation, T.-Y.C. and T.-L.W.; writing—review and editing, J.-H.H., W.-C.P., N.R., U.C., K.B., J.V.H. and T.-L.W.; supervision, N.R. and T.-L.W.; project administration, N.R. and T.-L.W.; funding acquisition, T.-L.W. All authors have read and agreed to the published version of the manuscript.

Funding: This work was financially supported by the "Advanced Semiconductor Technology Research Center" from The Featured Areas Research Center Program within the framework of the Higher Education Sprout Project by the Ministry of Education (MOE) in Taiwan. This work was also partly supported by the Ministry of Science and Technology, Taiwan, under Grant MOST 111-2634-F-A49-008, 111-2622-8-A49-018-SB, and 112-2636-E-A49-005.

Institutional Review Board Statement: Not applicable.

Informed Consent Statement: Not applicable.

Data Availability Statement: The data presented in this study are available upon request from the corresponding author. The data are not publicly available due to privacy.

Acknowledgments: This work was financially supported by the "Advanced Semiconductor Technology Research Center" from The Featured Areas Research Center Program within the framework of the Higher Education Sprout Project by the Ministry of Education (MOE) in Taiwan. This work was also partly supported by the Ministry of Science and Technology, Taiwan, under Grant MOST 111-2634-F-A49-008, 111-2622-8-A49-018-SB, and 112-2636-E-A49-005.

Conflicts of Interest: The authors declare no conflict of interest.

References

1. Böscke, T.S.; Müller, J.; Bräuhaus, D.; Schröder, U.; Böttger, U. Ferroelectricity in hafnium oxide thin films. *Appl. Phys. Lett.* **2011**, *99*, 102903. [CrossRef]
2. Song, C.M.; Kwon, H.J. Ferroelectrics based on HfO_2 film. *Electronics* **2021**, *10*, 2759. [CrossRef]
3. Müller, J.; Böscke, T.S.; Schröder, U.; Mueller, S.; Bräuhaus, D.; Böttger, U.; Frey, L.; Mikolajick, T. Ferroelectricity in Simple Binary ZrO_2 and HfO_2. *Nano Lett.* **2012**, *12*, 4318–4323. [CrossRef] [PubMed]
4. Cheema, S.S.; Kwon, D.; Shanker, N.; Reis, R.D.; Hsu, S.-L.; Xiao, J.; Zhang, H.; Wagner, R.; Datar, A.; McCarter, M.R.; et al. Enhanced ferroelectricity in ultrathin films grown directly on silicon. *Nature* **2020**, *580*, 478–482. [CrossRef] [PubMed]
5. Banerjee, W. Challenges and Applications of Emerging Nonvolatile Memory Devices. *Electronics* **2020**, *9*, 1029. [CrossRef]
6. Salahuddin, S.; Datta, S. Use of negative capacitance to provide voltage amplification for low power nanoscale devices. *Nano Lett.* **2008**, *8*, 405–410. [CrossRef] [PubMed]
7. Chou, C.-P.; Lin, Y.-X.; Huang, Y.-K.; Chan, C.-Y.; Wu, Y.-H. Junctionless Poly-GeSn Ferroelectric Thin-Film Transistors with Improved Reliability by Interface Engineering for Neuromorphic Computing. *ACS Appl. Mater. Interfaces* **2019**, *12*, 1014–1023. [CrossRef] [PubMed]
8. MKim, M.K.; Lee, J.S. Ferroelectric analog synaptic transistors. *Nano Lett.* **2019**, *19*, 2044–2050. [CrossRef]
9. Jerry, M.; Chen, P.Y.; Zhang, J.; Sharma, P.; Ni, K.; Yu, S.; Datta, S. Ferroelectric FET analog synapse for acceleration of deep neural network training. In Proceedings of the 2017 IEEE International Electron Devices Meeting (IEDM), San Francisco, CA, USA, 2–6 December 2017; pp. 6.2.1–6.2.4. [CrossRef]
10. Kimura, H.; Hanyu, T.; Kameyama, M.; Fujimori, Y.; Nakamura, T.; Takasu, H. Complementary ferroelectric-capacitor logic for low-power logic-in-memory VLSI. *IEEE J. Solid-State Circuits* **2004**, *39*, 919–926. [CrossRef]
11. Wang, Y.Y.; Wang, K.C.; Wu, C.H.; Chang, T.Y.; Ronchi, N.; Banerjee, K.; Van den Bosch, G.; Van Houdt, J.; Wu, T.L. Demonstration of 64 Conductance States and Large Dynamic Range in Si-doped HfO_2 FeFETs under Neuromorphic Computing Operations. In Proceedings of the 2022 International Symposium on VLSI Technology, Systems and Applications (VLSI-TSA), Hsinchu, Taiwan, 18–21 April 2022; pp. 1–2. [CrossRef]
12. Chen, Y.H.; Su, C.J.; Hu, C.; Wu, T.L. Effects of Annealing on Ferroelectric Hafnium Zirconium Oxide-Based Transistor Technology. *IEEE Electron Device Lett.* **2019**, *40*, 467–470. [CrossRef]
13. Cao, R.; Wang, Y.; Zhao, S.; Yang, Y.; Zhao, X.; Wang, W.; Zhang, X.; Lv, H.; Liu, Q.; Liu, M. Effects of Capping Electrode on Ferroelectric Properties of $Hf_{0.5}Zr_{0.5}O_2$ Thin Films. *IEEE Electron Device Lett.* **2018**, *39*, 1207–1210. [CrossRef]
14. Ronchi, N.; Ragnarsson, L.Å.; Breuil, L.; Banerjee, K.; McMitchell, S.R.C.; O'Sullivan, B.; Milenin, A.; Kundu, S.; Pak, M.; Van Houdt, J. Ferroelectric FET with Gd-doped HfO_2: A Step Towards Better Uniformity and Improved Memory Performance. In Proceedings of the 2021 Silicon Nanoelectronics Workshop (SNW), Kyoto, Japan, 13 June 2021; pp. 1–2.
15. Skopina, E.V.; Guillaume, N.; Alrifai, L.; Gonon, P.; Bsiesya, A. Sub-10-nm ferroelectric Gd-doped HfO_2 layers. *Appl. Phys. Lett.* **2022**, *120*, 172901. [CrossRef]
16. Tashiro, Y.; Shimizu, T.; Mimura, T.; Funakubo, H. Comprehensive Study on the Kinetic Formation of the Orthorhombic Ferroelectric Phase in Epitaxial Y-Doped Ferroelectric HfO_2 Thin Films. *ACS Appl. Electron. Mater.* **2021**, *3*, 3123–3130. [CrossRef]
17. Li, S.; Zhou, D.; Shi, Z.; Hoffmann, M.; Mikolajick, T.; Schroeder, U. Temperature-Dependent Subcycling Behavior of Si-Doped HfO_2 Ferroelectric Thin Films. *ACS Appl. Electron. Mater.* **2021**, *3*, 2415–2422. [CrossRef]
18. Wu, C.-H.; Wang, K.-C.; Wang, Y.-Y.; Hu, C.; Su, C.-J.; Wu, T.-L. Enhancement of Ferroelectricity in 5 nm Metal-Ferroelectric -Insulator Technologies by Using a Strained TiN Electrode. *Nanomaterials* **2022**, *12*, 468. [CrossRef]
19. Wu, C.-H.; Ronchi, N.; Wang, K.-C.; Wang, Y.-Y.; McMitchel, S.; Banerjee, K.; Van den Bosch, G.; Van Houdt, J.; Wu, T.-L. Impacts of Pulsing Schemes on the Endurance of Ferroelectric Metal–Ferroelectric–Insulator–Semiconductor Capacitors. *IEEE J. Electron Devices Soc.* **2022**, *10*, 109–114. [CrossRef]
20. Popovici, M.I.; Bizindavyi, J.; Favia, P.; Clima, S.; Alam, M.N.K.; Ramachandran, R.K.; Walke, A.M.; Celano, U.; Leonhardt, A.; Mukherjee, S.; et al. High performance La-doped HZO based ferroelectric capacitors by interfacial engineering. In Proceedings of the 2022 International Electron Devices Meeting (IEDM), San Francisco, CA, USA, 3–7 December 2022.
21. Tan, A.J.; Liao, Y.-H.; Wang, L.-C.; Shanker, N.; Bae, J.-H.; Hu, C.; Salahuddin, S. Ferroelectric HfO_2 Memory Transistors with High-κ Interfacial Layer and Write Endurance Exceeding 1010 Cycles. *IEEE Electron Device Lett.* **2021**, *42*, 994–997. [CrossRef]
22. Zagni, N.; Puglisi, F.M.; Pavan, P.; Alam, M.A. Reliability of HfO_2-Based Ferroelectric FETs: A Critical Review of Current and Future Challenges. *Proc. IEEE* **2023**, *111*, 158–184. [CrossRef]
23. Ronchi, N.; Ragnarsson, L.Å.; Celano, U.; Kaczer, B.; Kaczmarek, K.; Banerjee, K.; McMitchell, S.R.C.; Van Houdt, J. A comprehensive variability study of doped HfO_2 FeFET for memory applications. In Proceedings of the 2022 IEEE International Memory Workshop (IMW), Dresden, Germany, 15–18 May 2022.
24. Wei, X.K.; Sluka, T.; Fraygola, B.; Feigl, L.; Du, H.; Jin, L.; Setter, N. Controlled charging of ferroelastic domain walls in oxide ferroelectrics. *ACS Appl. Mater. Interfaces* **2017**, *9*, 6539–6546. [CrossRef] [PubMed]